Modeling Ultrasound Imaging as a Linear, Shift-Variant System

James Ng, Richard Prager, Nick Kingsbury, *Member, IEEE*, Graham Treece, and Andrew Gee

Abstract—We solve the equation that governs acoustic wave propagation in an inhomogeneous medium to show that the radio-frequency (RF) ultrasound signal can be expressed as the result of filtering the scatterer field with a point-spread function. We extend the analysis to make the link between the RF ultrasound signal and the representation of ultrasound scatterers as vectors with small magnitude and random phase in the complex plane. Others have previously performed parts of this analysis. The contribution of the present paper is to provide a single, coherent treatment emphasizing the assumptions that have to be made and the physical consequences of the models derived. This leads to insights into the interaction of monopole and dipole scattering, useful techniques for simulating and analyzing speckle statistics in the complex plane and a new expression for the normalized covariance of the analytic RF ultrasound signal in terms of the complex envelope of the point-spread function.

I. INTRODUCTION

IN this report, we demonstrate how a linear, shift-variant description of ultrasound imaging can be obtained by solving, under certain assumptions, the equation that governs wave propagation in an inhomogeneous medium. The theory of linear systems is well developed and well established in signal processing; a linear description is thus useful for casting ultrasound imaging into a framework that is well understood and for which mathematical tools already exist.

We then convert our linear model to complex analytic representation and derive the standard result whereby speckle is viewed as the result of constructive and destructive interference of a large number of vectors with random phase in the complex plane. From this, the first and second order statistics of fully developed speckle can be derived.

A number of other authors have published work in this area. The paper by Gore and Leeman [1] is one of the first publications to have developed a realistic model for ultrasonic backscattering in human tissue by assuming weak scattering and a windowed monochromatic separable incident pulse. A more thorough analysis was carried out by Jensen [2], who derived the wave equation from first principles and solved it to obtain an analytic expression for the backscattered radio-frequency (RF) trace in the time domain. Zemp *et al.* [3] provided an overview of the solution of the wave equation and extended the linear model further to the computation of signal statistics.

Our analysis here is similar to the treatments by Gore and Leeman [1] and by Jensen [2]. Like Jensen, our aim is to express the backscattered RF trace as the result of linearly filtering a map of the acoustic inhomogeneities in the imaged region by a transfer function determined by the geometry and mechanics of the ultrasonic transceiving probe. However, we have taken the extra step of proving that, for the special case of a rectilinear scanning geometry and neglecting edge effects, the point-spread function (PSF) of the imaging system is shift-variant only in the axial direction. We restrict ourselves to consider linear wave propagation only. Modern clinical practice sometimes exploits higher-order harmonics generated by nonlinearities during transmission. We note a comment in [3] that, although the forward propagation of waves in such a case is nonlinear, a linear model would still hold for the back propagation provided that the scattering is weak (which is usually the case in soft tissue).

Many authors use a complex model for the analysis of speckle [4]–[7], relying on an analogy with the theory of laser speckle for justification [8]. We are not aware of an explicit presentation of the link between the RF ultrasound signal and its representation in the complex plane. Therefore, this is covered in some detail in the present paper to show the assumptions on which it is based and the relationships between the complex quantities and their analogues in the real world.

II. BACKGROUND

Conventional ultrasound imaging interrogates a medium with high-frequency, band-limited acoustic waves and detects echoes scattered by inhomogeneities (also referred to as scatterers) within the medium. A single probe placed in contact with the subject is used for both the generation of these waves and the reception of their echoes. On the contact surface of a typical probe is found an array of piezoelectric crystals or elements (referred to as the aperture), each of which behaves as an electromechanical transducer. A focused beam is produced by coherently exciting a set of adjacent elements that we refer to as the transmit subaperture. In a similar way, backscattered echoes are detected by adjacent elements in the receive subaperture; these echoes are then coherently summed, and the result is

filtered to produce a single RF voltage trace [2], [3][1]. For the sake of simplicity, we restrict our discussion in this paper to a rectilinear scanning geometry, in which multiple, parallel RF traces are acquired by laterally translating the transmit and receive subapertures.

At each transmission, the emitted wave propagating through the medium gives rise to an incident pressure field, and the scattered waves give rise to a scattered pressure field. It can be shown that, at any moment in time, the total pressure field is the sum of these two fields (see Section III-A). To minimize sidelobes in the transmit-receive response of the probe, apodization (i.e., amplitude weighting of the elements in the subapertures) is often applied.

III. The Wave Equation

With the physical description of the previous section in mind, we shall proceed in this section to develop mathematical expressions for the incident pressure field and the scattered pressure field. Our analysis necessarily begins by considering the partial differential equation (PDE) that describes the propagation of acoustic waves in a nonuniform medium. We shall use the wave equation that is found in [1] and [9], in which the acoustic properties of the medium are specified in terms of its density and adiabatic compressibility. We restrict ourselves to the case of weak scattering in which the energy of the scattered waves is much less than the energy of the incident waves.

To simplify the mathematics, the wave equation and its solution will be expressed in terms of angular frequency ω instead of time t; although less intuitive, this representation has the advantage of improving notational clarity by reducing convolutions in the time domain to multiplications in the frequency domain. The vector $\mathbf{x}$ will be used to represent the coordinates (x, y, z) of three-dimensional space. (A complete list of symbols is given in Table I.)

A. The Total Pressure Field

In the absence of any scatterers, we consider our medium to be uniform with density ρ_o and adiabatic compressibility κ_0. The speed c_0 at which acoustic waves travel in this uniform medium is given by [9]:

$$c_0 = \frac{1}{\sqrt{\rho_0 \kappa_0}}. \tag{1}$$

The presence of scatterers in the medium may be modeled by adding spatially-dependent terms $\Delta\rho(\mathbf{x})$ and $\Delta\kappa(\mathbf{x})$ to the density and the compressibility, respectively. Without proof, we state that the total pressure field $P'(\mathbf{x}, \omega)$ that develops as a result of acoustic wave propagation obeys the linear PDE [1], [9]:

[1]M. E. Anderson and G. E. Trahey, "A seminar on k-space applied to medical ultrasound," Apr. 2000, available: http://dukemil.egr.duke.edu/Ultrasound/k-space/bme265.htm [Dec. 15, 2004].

$$\nabla^2 P'(\mathbf{x}, \omega) + \left(\frac{\omega}{c_0}\right)^2 P'(\mathbf{x}, \omega) = -(\mathbf{S}P')(\mathbf{x}, \omega), \tag{2}$$

where $\mathbf{S}$ is the scattering operator defined as

$$\mathbf{S} \equiv \gamma(\mathbf{x}) \left(\frac{\omega}{c_0}\right)^2 - \nabla \cdot \mu(\mathbf{x})\nabla, \tag{3}$$

and the scattering terms $\gamma(\mathbf{x})$ and $\mu(\mathbf{x})$ are defined as:

$$\gamma(\mathbf{x}) \equiv \frac{\Delta\kappa(\mathbf{x})}{\kappa_0}, \ \mu(\mathbf{x}) \equiv \frac{\Delta\rho(\mathbf{x})}{\rho_0 + \Delta\rho(\mathbf{x})}. \tag{4}$$

In keeping with the definitions introduced by Andersen and Trahey[1], the term $\gamma(\mathbf{x})$ contributes monopole radiation and $\mu(\mathbf{x})$ contributes dipole radiation.

Although (2) is, strictly speaking, homogeneous [there are no terms independent of $P'(\mathbf{x}, \omega)$], we shall nevertheless treat it as an inhomogeneous PDE and treat the nonzero, right-hand side (RHS) as a source term. This is acceptable because, in a sense, the RHS represents the source of scattered sound [9].

Because (2) is linear, we can write its general solution as the sum of the solution to the corresponding homogeneous equation (i.e., with the RHS set to zero) and any particular solution [10]. Denoting the solution to the homogeneous equation as $P_i(\mathbf{x}, \omega)$ and the particular solution as $P_s(\mathbf{x}, \omega)$, we, therefore, can write the total field as:

$$P'(\mathbf{x}, \omega) = P_i(\mathbf{x}, \omega) + P_s(\mathbf{x}, \omega). \tag{5}$$

To assign a physical interpretation to $P_i(\mathbf{x}, \omega)$, we observe that, by setting the RHS of (2) to zero, we have effectively set $\Delta\rho(\mathbf{x}) = \Delta\kappa(\mathbf{x}) = 0$. We see then that $P_i(\mathbf{x}, \omega)$ is the pressure field that develops in the absence of any scatterers which, by definition, is the incident pressure field. We also know that the scattered pressure field must obey (2), and so we can assign our particular solution $P_s(\mathbf{x}, \omega)$ to be the scattered pressure field. With these physical interpretations for $P_i(\mathbf{x}, \omega)$ and $P_s(\mathbf{x}, \omega)$, we see that (5) confirms the statement in Section II that the total pressure field is the sum of the incident pressure field and the scattered pressure field.

B. The Incident Pressure Field

Calculating the incident pressure field requires knowledge of the mechanics and geometry of the probe. We adopt the generalized, three-dimensional coordinate system shown in Fig. 1, where:

- $\mathcal{A}$ is a surface bounding the transmit and receive subapertures.
- $\mathbf{x_0}$ is the location of the center of $\mathcal{A}$.
- $\mathbf{x_a}$ is an arbitrary point on $\mathcal{A}$.
- $\mathcal{V}$ is a volume within which the scatterers being considered are contained.
- $\mathbf{x}'$ is an arbitrary point in $\mathcal{V}$.

The surface $\mathcal{A}$ may be considered to consist of infinitesimally small area elements $d^2\mathbf{x_a}$, each of which behaves

TABLE I

LIST OF SYMBOLS

|	
$\underset{t}{\otimes}$	Convolution with respect to t
$\underset{\mathbf{x}}{\otimes}$	Convolution with respect to $\mathbf{x}$
$\langle\bullet\rangle$	Expected value of a quantity
$\mathcal{A}$	Surface bounding the transmit and receive subapertures
A_1 and A_2	Amplitude of the signal at points 1 and 2
c_0	Speed of sound in a homogeneous medium
$E_m(\omega)$ or $e_m(t)$	Electromechanical transfer function/impulse response
$E(\bullet)$	Complete elliptic integral of the second kind
$\mathcal{F}^{-1}\{\bullet\}$	Inverse temporal Fourier transform
$F(\mathbf{x_0},\omega)$	Force on the receive subaperture
$f_m(\mathbf{x})$ or $f_m(x,y,z)$	Scatterer field
$\tilde{f}_m(x,y,z)$	Amplitude from scatterer field, random phase
$_2F_1(\bullet)$	Gaussian hypergeometric function
$h(\mathbf{x},t)$ or $h(x,y,z,t)$	PSF of the imaging system
$h_{pe}(\mathbf{x},t)$	Pulse-echo impulse response
$H_r(\mathbf{x},\omega)$	Receive transfer function
$H_t(\mathbf{x},\omega)$	Transmit transfer function
$\tilde{h}(x,y,z,t)$	Complex envelope of the point spread function
$\mathcal{H}_t\{\bullet\}$	Hilbert transform in time
$\Im(\bullet)$	Imaginary part of a number
I_1 and I_2	Intensity of signal at points 1 and 2
$K(\bullet)$	Complete elliptic integral of the first kind
k_0	Spatial frequency or wave number
$P'(\mathbf{x},\omega)$	Total pressure field
$P_i(\mathbf{x},\omega)$ or $P_i(\mathbf{x},\mathbf{x_0},\omega)$	Incident pressure field
$P_s(\mathbf{x},\omega)$ or $P_s(\mathbf{x},\mathbf{x_0},\omega)$	Scattered pressure field
$\mathbf{Pr}(\bullet)$	Probability of a particular value
R^3	Three-dimensional space
$R(\mathbf{x_0},\omega)$ or $r(\mathbf{x_0},t)$ or $r(x,y,t)$	RF Voltage trace
$\tilde{r}(x,y,t)$	Base-band analytic RF signal
$\Re(\bullet)$	Real part of a number
$\mathbf{S}$	Scattering operator
t	Time coordinate
$\mathcal{V}$	Volume containing scatterers
$V(\mathbf{x_a},\omega)$	Position-dependent normal velocity over $\mathcal{A}$
$V_{pe}(\omega)$ or $v_{pe}(t)$	Pulse-echo wavelet
w_x	Std. deviation width in x dir. of Gaussian resolution cell
$\mathbf{x}$	Position vector in three-dimensional space
$\mathbf{x}'$	Point in V; also a dummy variable of integration
$\mathbf{x_0}$	Center of $\mathcal{A}$
$\mathbf{x_a}$	Point on $\mathcal{A}$
$\gamma(\mathbf{x})$	Compressibility (monopole) scattering term
$\Delta\kappa(\mathbf{x})$	Change in compressibility introduced by scatterers
$\Delta\rho(\mathbf{x})$	Change in density introduced by scatterers
δ_x	A small displacement in the x direction
κ_0	Uniform compressibility in a homogeneous medium
λ	Magnitude of normalized covariance of $\tilde{r}(x,y,z,t)$
$\mu(\mathbf{x})$	Density (dipole) scattering term
ρ_0	Uniform density in a homogeneous medium
$\rho(p,q)$	Pearson correlation coefficient between p and q
σ	Standard deviation of the probability distribution
$W(\mathbf{x_a},\omega)$	Weighting term on elements in the receive subaperture
ω	Temporal angular frequency
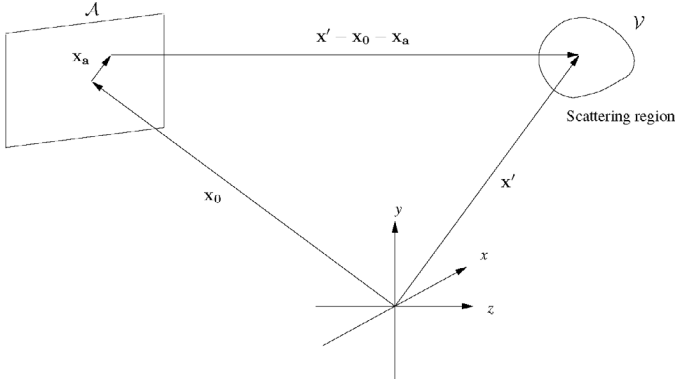
Fig. 1. Coordinate system for describing scattering in an inhomogeneous medium.

as a simple point source mounted on a rigid baffle. The Huygen-Fresnel principle states that each area element contributes a spherically expanding wave to the incident pressure field[1]. Therefore, the incident pressure field may be obtained by summing the spherical wave contribution from each area element.

If we assume that the radius of curvature of $\mathcal{A}$ is large enough that $\mathcal{A}$ may be considered to be effectively flat, we can express the incident pressure field as the Rayleigh integral [2], [9], [11], [12]:

$$P_i \left(\mathbf{x}, \mathbf{x_0}, \omega \right) = \frac{\rho_0}{2\pi} \int_{\mathcal{A}} j\omega V \left(\mathbf{x_a}, \omega \right) \frac{e^{-j\frac{\omega}{c_0} |\mathbf{x} - \mathbf{x_0} - \mathbf{x_a}|}}{|\mathbf{x} - \mathbf{x_0} - \mathbf{x_a}|} d^2\mathbf{x_a}, \quad (6)$$

where $V \left(\mathbf{x_a}, \omega \right)$ is the temporal Fourier transform of the normal velocity on the transmit subaperture's surface; this normal velocity is not uniform but varies from point to point on $\mathcal{A}$. We note that the term $j\omega V \left(\mathbf{x_a}, \omega \right)$ corresponds to the normal acceleration in the time domain because the factor $j\omega$ corresponds to time differentiation. We have implicitly incorporated the effects of focusing and apodization into $V \left(\mathbf{x_a}, \omega \right)$, which may be complex valued.

Although we have stated (6) without proof, we can intuitively see that it is indeed the Huygen-Fresnel principle expressed mathematically: the integral on the RHS describes the summation of complex-valued, spherically expanding waves, each weighted by the normal acceleration at its source and decaying in amplitude with increasing distance from its source.

For convenience, we define a new quantity $H_t(\mathbf{x}, \omega)$ that, for reasons which will become clear, we shall refer to as the transmit transfer function:

$$H_t(\mathbf{x}, \omega) \equiv \int_{\mathcal{A}} V \left(\mathbf{x_a}, \omega \right) \frac{e^{-j\frac{\omega}{c_0} |\mathbf{x} - \mathbf{x_a}|}}{2\pi |\mathbf{x} - \mathbf{x_a}|} d^2\mathbf{x_a}, \quad (7)$$

(6) then can be expressed more compactly as:

$$P_i \left(\mathbf{x}, \mathbf{x_0}, \omega \right) = j\omega\rho_0 H_t \left(\mathbf{x} - \mathbf{x_0}, \omega \right). \quad (8)$$

The quantity $H_t(\mathbf{x}, \omega)$, into which are incorporated the effects of apodization and focusing, accounts entirely for the spatial distribution of the incident pressure field.

C. The Scattered Pressure Field

To calculate the scattered pressure field, we solve (2) by using the Green's function method. We consider the waves scattered from the volume $\mathcal{V}$ to be propagating into an effectively unbounded medium, in which case the Green's function takes the form $\frac{-1}{4\pi|\mathbf{x}-\mathbf{x'}|} \exp\left(-j\frac{\omega}{c_0} |\mathbf{x} - \mathbf{x'}| \right)$ [13]. The particular solution to (2) is then the product of the RHS and the Green's function integrated over the volume $\mathcal{V}$ [1], [9], [13]. Furthermore, if we define $\Delta\rho(\mathbf{x})$ and $\Delta\kappa(\mathbf{x})$ to be zero outside $\mathcal{V}$, then we can perform the integration over all of the three-dimensional space, and the scattered pressure field can be expressed as the convolution integral:

$$P_s \left(\mathbf{x}, \mathbf{x_0}, \omega \right) = \int_{\mathbb{R}^3} \left(\mathbf{S}P' \right) \left(\mathbf{x'}, \mathbf{x_0}, \omega \right) \frac{e^{-j\frac{\omega}{c_0} |\mathbf{x}-\mathbf{x'}|}}{4\pi |\mathbf{x} - \mathbf{x'}|} d^3\mathbf{x'}. \quad (9)$$

Because we are dealing only with the case of weak scattering, we assume that $|P_s \left(\mathbf{x}, \mathbf{x_0}, \omega \right)| \ll |P_i \left(\mathbf{x}, \mathbf{x_0}, \omega \right)|$. $P_s \left(\mathbf{x}, \mathbf{x_0}, \omega \right)$ in (5) then becomes negligible and $P' \left(\mathbf{x}, \mathbf{x_0}, \omega \right) \approx P_i \left(\mathbf{x}, \mathbf{x_0}, \omega \right)$. Rewriting (9) with $P' \left(\mathbf{x}, \mathbf{x_0}, \omega \right)$ substituted by $P_i \left(\mathbf{x}, \mathbf{x_0}, \omega \right)$:

$$P_s \left(\mathbf{x}, \mathbf{x_0}, \omega \right) \approx \int_{\mathbb{R}^3} \left(\mathbf{S}P_i \right) \left(\mathbf{x'}, \mathbf{x_0}, \omega \right) \frac{e^{-j\frac{\omega}{c_0} |\mathbf{x}-\mathbf{x'}|}}{4\pi |\mathbf{x} - \mathbf{x'}|} d^3\mathbf{x'}. \quad (10)$$

This approximation is referred to as the (first) Born approximation [1], [2], [9], [11], [12], and (10) states that the scattered pressure field is, to a first approximation, the spherically-expanding wave $\frac{1}{4\pi|\mathbf{x}|} \exp\left(-j\frac{\omega}{c_0} |\mathbf{x}| \right)$ convolved onto the scattering term $\left(\mathbf{S}P_i \right) \left(\mathbf{x}, \mathbf{x_0}, \omega \right)$. If we regard the scatterers to be idealized points in $\mathcal{V}$, this is equivalent to saying that these point scatterers each contribute a spherically expanding wave independently of each other. Thus, in making the Born approximation, we have assumed implicitly that multiply scattered waves (i.e., waves scattered off a particle that are then scattered off other particles) are negligible, and that multiple scattering can be ignored [1], [2], [12].

By substituting the expression for $P_i(\mathbf{x}, \mathbf{x_0}, \omega)$ in (8) into (10), the scattered field can be expressed entirely in terms of the probe's characteristics and the scattering operator:

$$P_s \left(\mathbf{x}, \mathbf{x_0}, \omega \right) \approx j\omega\rho_0 \int_{\mathbb{R}^3} \left(\mathbf{S}H_t \right) \left(\mathbf{x'} - \mathbf{x_0}, \omega \right) \frac{e^{-j\frac{\omega}{c_0} |\mathbf{x}-\mathbf{x'}|}}{4\pi |\mathbf{x} - \mathbf{x'}|} d^3\mathbf{x'}. \quad (11)$$

D. The Force on the Receive Subaperture

We recall from the physical description in Section II that the received RF voltage trace is obtained by summing the scattered pressure field over the receive subaperture and filtering this sum by the electromechanical response of the piezoelectric elements. In this subsection, we compute the summation of the scattered pressure field over the receive subaperture. Strictly speaking, this quantity,

which will be denoted by $F(\mathbf{x_0}, \omega)$, is the force exerted on the receive subaperture [3].

If we represent the apodization and focusing on reception collectively in a single complex-valued term $W(\mathbf{x_a}, \omega)$, then:

$$F(\mathbf{x_0}, \omega) = \int_{\mathcal{A}} W(\mathbf{x_a}, \omega) P_s(\mathbf{x_0} + \mathbf{x_a}, \mathbf{x_0}, \omega) d^2\mathbf{x_a}. \tag{12}$$

Substituting in the integral expression for $P_s(\mathbf{x_0} + \mathbf{x_a}, \mathbf{x_0}, \omega)$ from (11) yields (13) (see next page). For convenience, we define another new quantity $H_r(\mathbf{x}, \omega)$ that we shall refer to as the receive transfer function:

$$H_r(\mathbf{x}, \omega) \equiv \int_{\mathcal{A}} W(\mathbf{x_a}, \omega) \frac{e^{-j\frac{\omega}{c_0}|\mathbf{x}-\mathbf{x_a}|}}{4\pi|\mathbf{x}-\mathbf{x_a}|} d^2\mathbf{x_a}. \tag{14}$$

Hence, we can write (13) as:

$$F(\mathbf{x_0}, \omega) \approx j\omega\rho_0 \int_{\mathsf{R}^3} (\mathbf{S}H_t)(\mathbf{x}'-\mathbf{x_0}, \omega) H_r(\mathbf{x}'-\mathbf{x_0}, \omega) d^3\mathbf{x}'. \tag{15}$$

At this point, we substitute in the definition of the scattering operator $\mathbf{S}$ from (3) to get:

$$F(\mathbf{x_0}, \omega) \approx$$
$$j\omega\rho_0 \left\{ \left(\frac{\omega}{c_0}\right)^2 \int_{\mathsf{R}^3} \gamma(\mathbf{x}') H_t(\mathbf{x}'-\mathbf{x_0}, \omega) H_r(\mathbf{x}'-\mathbf{x_0}, \omega) d^3\mathbf{x}' \right.$$
$$\left. - \int_{\mathsf{R}^3} \nabla \cdot [\mu(\mathbf{x}')(\nabla H_t)(\mathbf{x}'-\mathbf{x_0}, \omega)] H_r(\mathbf{x}'-\mathbf{x_0}, \omega) d^3\mathbf{x}' \right\}. \tag{16}$$

To simplify the second integral on the RHS, we first note that (see Appendix A for a proof):

$$\int_{\mathsf{R}^3} \nabla \cdot [\mu(\mathbf{x})(\nabla H_t)(\mathbf{x}, \omega)] H_r(\mathbf{x}, \omega) d^3\mathbf{x} =$$
$$-\int_{\mathsf{R}^3} \mu(\mathbf{x})(\nabla H_t \cdot \nabla H_r)(\mathbf{x}, \omega) d^3\mathbf{x}, \tag{17}$$

and so we arrive at:

$$F(\mathbf{x_0}, \omega) \approx$$
$$j\omega\rho_0 \left\{ \left(\frac{\omega}{c_0}\right)^2 \int_{\mathsf{R}^3} \gamma(\mathbf{x}') H_t(\mathbf{x}'-\mathbf{x_0}, \omega) H_r(\mathbf{x}'-\mathbf{x_0}, \omega) d^3\mathbf{x}' \right.$$
$$\left. + \int_{\mathsf{R}^3} \mu(\mathbf{x}')(\nabla H_t \cdot \nabla H_r)(\mathbf{x}'-\mathbf{x_0}, \omega) d^3\mathbf{x}' \right\}. \tag{18}$$

At sufficiently large distances away from the surface $\mathcal{A}$, we can use the approximation (see Appendix B for a proof):

$$(\nabla H_t \cdot \nabla H_r)(\mathbf{x}-\mathbf{x_0}, \omega) \approx$$
$$-\left(\frac{\omega}{c_0}\right)^2 H_t(\mathbf{x}-\mathbf{x_0}, \omega) H_r(\mathbf{x}-\mathbf{x_0}, \omega). \tag{19}$$

This allows us to rewrite $F(\mathbf{x_0}, \omega)$ as:

$$F(\mathbf{x_0}, \omega) \approx \frac{j\omega^3\rho_0}{c_0^2} \times$$
$$\int_{\mathsf{R}^3} H_t(\mathbf{x}'-\mathbf{x_0}, \omega) H_r(\mathbf{x}'-\mathbf{x_0}, \omega) [\gamma(\mathbf{x}') - \mu(\mathbf{x}')] d^3\mathbf{x}'. \tag{20}$$

What exactly is meant by sufficiently large distances away from the surface $\mathcal{A}$ is discussed in detail in Appendix B. In short, (19) is well satisfied at axial depths greater than the diameter of $\mathcal{A}$ [11]; for noncircular $\mathcal{A}$, this is the diameter of the smallest circle within which $\mathcal{A}$ can be inscribed.

It may be instructive to also consider equations (18) and (20) from the point-of-view of linear systems. We refer to Fig. 2(a), which illustrates graphically how the signal $F(\mathbf{x_0}, \omega)$ is composed of monopole and dipole components [recall from Section III-A that $\gamma(\mathbf{x})$ and $\mu(\mathbf{x})$ are monopole and dipole terms, respectively]. From a systems' point-of-view, $\gamma(\mathbf{x})$ and $\mu(\mathbf{x})$ are two distinct input signals, each convolved with a different spatiotemporal filter before being summed up and temporally filtered to produce $F(\mathbf{x_0}, \omega)$. It is only at axial distances greater than the dimensions of $\mathcal{A}$ that the responses of the monopole and dipole spatiotemporal filters become sufficiently similar in magnitude for $\mu(\mathbf{x})$ and $\gamma(\mathbf{x})$ to be combined into a single input as shown in Fig. 2(b). In the special case that either monopole or dipole scattering is dominant, one of the branches in the block diagram of Fig. 2(a) is effectively rendered negligible, and the linear system depicted in this block diagram is reduced to having just one input signal.

In [14], an imaging method able to separate the monopole and dipole components of Rayleigh scattering is described, and it is claimed that such techniques can improve soft tissue contrast and add diagnostic value. Expression (18) is useful in this context to describe the blurrings of the separate density and compressibility images; accurate characterization of the blurrings would be useful in subsequent analysis and processing, especially for deconvolution.

E. The RF Voltage Trace

We now model the electromechanical conversion of the force on the receive subaperture into a voltage trace. If we define the electromechanical transfer function that models this conversion to be $E_m(\omega)$ and the voltage trace to be $R(\mathbf{x_0}, \omega)$, we have $R(\mathbf{x_0}, \omega) = E_m(\omega)F(\mathbf{x_0}, \omega)$ [2], [3]; substituting in the expression for $F(\mathbf{x_0}, \omega)$ from (20) we get:

$$R(\mathbf{x_0}, \omega) \approx \frac{j\omega^3\rho_0}{c_0^2} E_m(\omega) \times$$
$$\int_{\mathsf{R}^3} H_t(\mathbf{x}'-\mathbf{x_0}, \omega) H_r(\mathbf{x}'-\mathbf{x_0}, \omega) [\gamma(\mathbf{x}') - \mu(\mathbf{x}')] d^3\mathbf{x}'. \tag{21}$$

For convenience, we group the properties of the medium together and the electromechanical characteristics of the

$$
\begin{aligned}
F\left(\mathbf{x_0}, \omega\right) &\approx j\omega\rho_0 \int_{\mathcal{A}} W\left(\mathbf{x_a}, \omega\right) \left[\int_{\mathsf{R}^3} \frac{(\mathbf{S}H_t)\left(\mathbf{x'} - \mathbf{x_0}, \omega\right) e^{-j\frac{\omega}{c_0}\left|\mathbf{x_0} + \mathbf{x_a} - \mathbf{x'}\right|}}{4\pi \left|\mathbf{x_0} + \mathbf{x_a} - \mathbf{x'}\right|} d^3\mathbf{x'}\right] d^2\mathbf{x_a} \\
&\approx j\omega\rho_0 \int_{\mathsf{R}^3} (\mathbf{S}H_t)\left(\mathbf{x'} - \mathbf{x_0}, \omega\right) \left[\int_{\mathcal{A}} \frac{W\left(\mathbf{x_a}, \omega\right) e^{-j\frac{\omega}{c_0}\left|\mathbf{x_0} + \mathbf{x_a} - \mathbf{x'}\right|}}{4\pi \left|\mathbf{x_0} + \mathbf{x_a} - \mathbf{x'}\right|} d^2\mathbf{x_a}\right] d^3\mathbf{x'}.
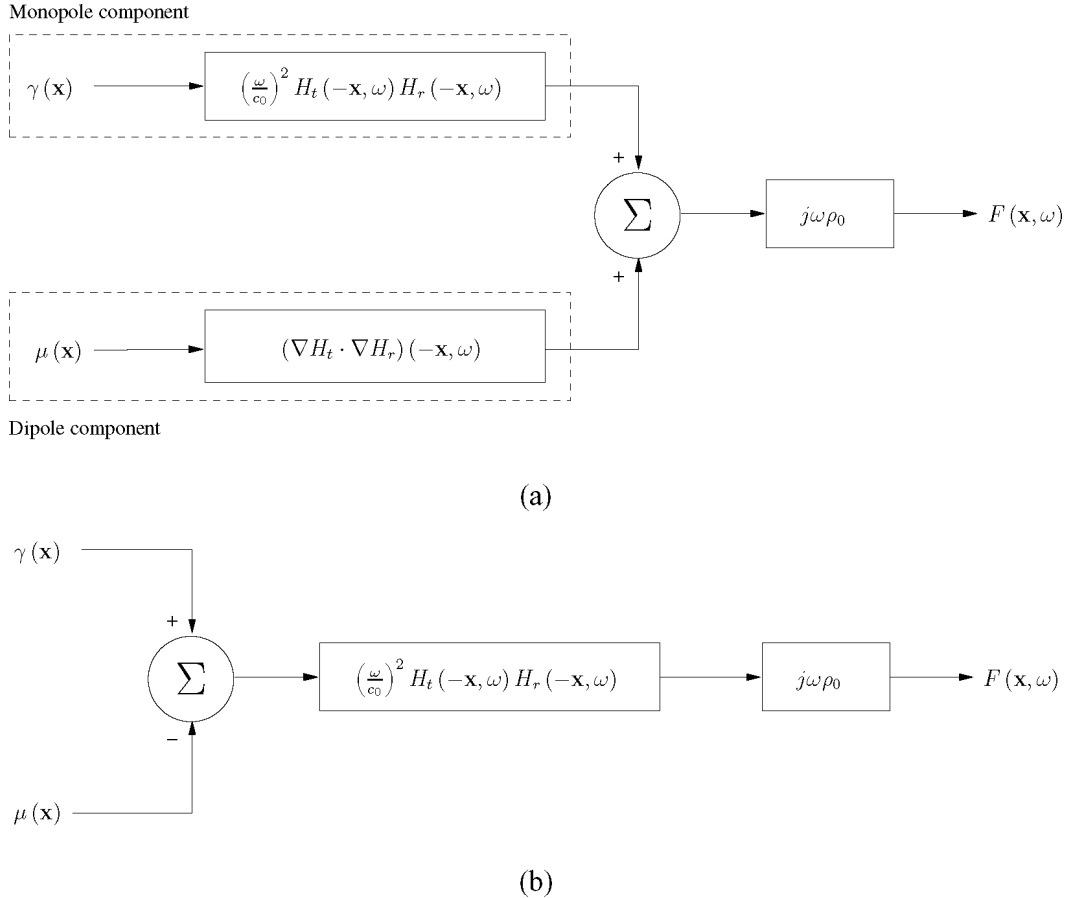\end{aligned}
\tag{13}
$$

Fig. 2. Block diagram representations of (a) (18) and (b) (20): (a) is valid close to $\mathcal{A}$ and shows that the force $F(\mathbf{x}, \omega)$ is composed of separate components related to monopole and dipole scattering; (b) shows how these two components can be combined for scattering at some distance away from $\mathcal{A}$.

probe together. We adopt definitions similar to those given in [2] and write the voltage trace as:

$$
R\left(\mathbf{x_0}, \omega\right) \approx V_{pe}\left(\omega\right) H_t(-\mathbf{x}, \omega) H_r\left(-\mathbf{x}, \omega\right)
$$

$$
\left. \underset{\mathbf{x}}{\otimes} f_m\left(\mathbf{x}\right) \right|_{\mathbf{x}=\mathbf{x_0}}, \tag{22}
$$

$$
V_{pe}(\omega) = j\omega^3 E_m(\omega), \tag{23}
$$

$$
f_m(\mathbf{x}) = \frac{\rho_0^2 \kappa_0}{2} \left[\frac{\Delta\kappa(\mathbf{x})}{\kappa_0} - \frac{\Delta\rho(\mathbf{x})}{\rho_0 + \Delta\rho(\mathbf{x})}\right]. \tag{24}
$$

We adopt similar terminology as in [2] and refer to the quantities $V_{pe}(\omega)$ and $f_m(\mathbf{x})$, respectively, as the pulse-echo wavelet and the tissue reflectivity or scatterer field. Note that, to obtain the expression for $f_m(\mathbf{x})$ in (24), we have substituted in the definitions of c_0, $\gamma(\mathbf{x})$ and $\mu(\mathbf{x})$

from (1) and (4). We note from [3] that, provided $\Delta\kappa(\mathbf{x})$ and $\Delta\rho(\mathbf{x})$ are small, $f_m(\mathbf{x})$ may be approximately regarded as the spatial variation in the medium's acoustic impedance.

We also can express the voltage trace in the time domain as:

$$
\left. r\left(\mathbf{x_0}, t\right) \approx v_{pe}(t) \underset{t}{\otimes} h_{pe}(-\mathbf{x}, t) \underset{\mathbf{x}}{\otimes} f_m(\mathbf{x}) \right|_{\mathbf{x}=\mathbf{x_0}}, \tag{25}
$$

$$
v_{pe}(t) = \mathcal{F}^{-1}\left\{V_{pe}(\omega)\right\} = -\frac{d^3 e_m}{dt^3} \tag{26}
$$

$$
h_{pe}(\mathbf{x}, t) = \mathcal{F}^{-1}\left\{H_t(\mathbf{x}, \omega) H_r(\mathbf{x}, \omega)\right\}, \tag{27}
$$

$$
e_m(t) = \mathcal{F}^{-1}\left\{E_m(\omega)\right\}. \tag{28}
$$

If we regard the quantity $f_m(\mathbf{x})$ as the input signal and $r\left(\mathbf{x_0}, t\right)$ as the output signal, (22) and (25) show that the
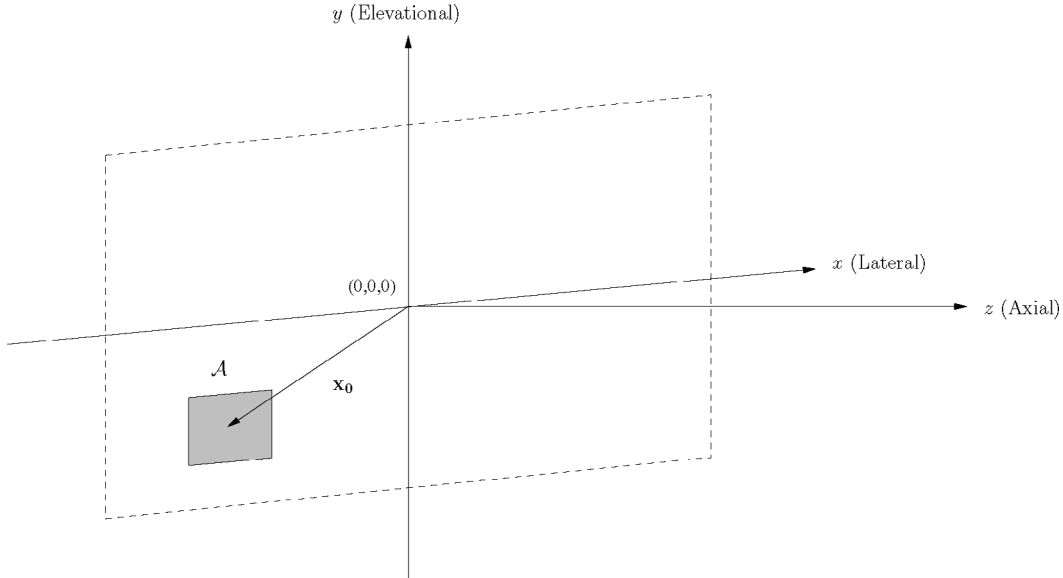
Fig. 3. Coordinate system for demonstrating the shift variance of the PSF in the axial direction.

imaging system is linear with a spatiotemporal transfer function $V_{pe}(\omega)H_t(-\mathbf{x},\omega)H_r(-\mathbf{x},\omega)$ or impulse response $v_{pe}(t)\underset{t}{\otimes}h_{pe}(-\mathbf{x},t)$. Our definition of the transfer function of the imaging system in this way neatly distinguishes between the electromechanical characteristics of the probe (represented by the pulse-echo wavelet $V_{pe}(\omega)$) and the geometry of the probe (represented by the pulse-echo transfer function $H_t(-\mathbf{x},\omega)H_r(-\mathbf{x},\omega)$).

IV. Shift Variance in the Axial Direction

To view ultrasound imaging from a purely signal processing point-of-view, we can combine the electromechanical response $v_{pe}(t)$ and the pulse-echo impulse response $h_{pe}(\mathbf{x},t)$ into a PSF. If we formally define $h(\mathbf{x},t) = v_{pe}(t)\underset{t}{\otimes}h_{pe}(\mathbf{x},t)$, then:

$$r(\mathbf{x_0},t) \approx h(-\mathbf{x},t) \underset{\mathbf{x}}{\otimes} f_m(\mathbf{x})\Big|_{\mathbf{x}=\mathbf{x_0}}, \qquad (29)$$

We can gain a little more insight into the behavior of the PSF by adopting the coordinate system shown in Fig. 3, in which the x, y, and z axes are aligned with the lateral, elevational, and axial directions, respectively.

In a rectilinear scanning geometry, a two-dimensional RF image is acquired by capturing RF traces at different lateral positions. A three-dimensional RF image is acquired by translating the probe in the elevational direction. Therefore, the vector $\mathbf{x_0}$ only changes laterally and elevationally (i.e., in the x and y directions only); its z coordinate never changes. Hence, without loss of generality, we can restrict the surface of $\mathcal{A}$ to lie on the xy plane. We then can write $\mathbf{x_0} = [x\ y\ 0]$ and $\mathbf{x} = [x\ y\ z]$, and (29) can be written out in full as:

$$r(x,y,t) \approx$$
$$\int\!\!\!\int\!\!\!\int_{-\infty}^{+\infty} h\left(x'-x, y'-y, z', t\right) f_m\left(x',y',z'\right) dx'dy'dz'. \quad (30)$$

We see from (30) that the PSF is shift variant along the axial direction but shift invariant along the lateral and elevational directions. This lateral and elevational shift invariance only hold when scanning in a rectilinear fashion. Furthermore, at the lateral edges of the probe at which there are an insufficient number of elements to form the full transmit and receive subapertures, the subapertures usually are truncated, distorting the PSF. Thus, the PSF is laterally shift invariant except at the lateral edges.

We present an example of a typical PSF in Fig. 4. We have included Fig. 4 to illustrate the axial variation in the PSF, particularly before and after the focal point. Notice that the PSF is more tightly focused in the lateral direction as the transmit-receive aperture width in this direction is much larger, with fewer sidelobes. This is typical of realistic probes, in which elevational focusing is achieved through an acoustic lens that cannot be apodized.

V. Complex Representation and Signal Statistics

Having derived an expression for $r(x,y,t)$ in terms of the point spread function and the scatterer field, most authors stop at this point and cite one of the classic texts on speckle [8] when they wish to talk about the echo envelope amplitude of diffuse scattering as analogous to the distance traveled by a random walk in the complex plane. In this section we go through the algebra that links the real RF signal with the corresponding analytic representation in the complex plane. This enables us to make clear the assumptions that are involved, and provides an explicit rela-
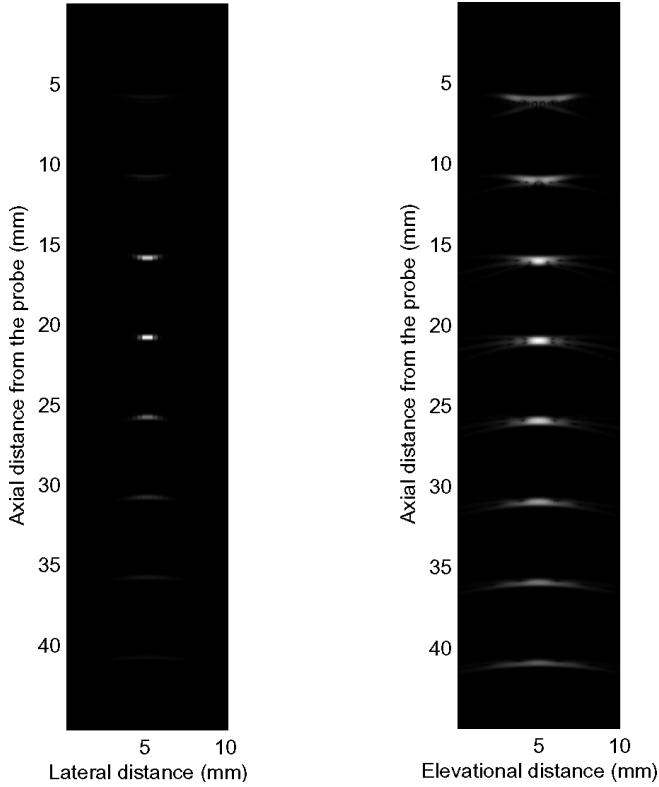
Fig. 4. Axial-lateral (left) and axial-elevational (right) cross sections of a typical system PSF at different axial depths from an apodized aperture after demodulation and logarithmic compression. This PSF was obtained by simulating the response of a 6.5 MHz, single-focus probe to a point scatterer at different axial depths in Field II [15]. The transmit and receive subapertures are identical, consisting of 32 elements, each measuring 0.3 mm (lateral) by 6 mm (elevational) with a lateral gap of 0.1 mm between adjacent elements. Hamming window apodization was applied. Both lateral and elevational focal lengths were set to 20 mm. The speed of sound was set to 1540 m/s.

tionship between the envelope of the point spread function $\tilde{h}(x, y, z, t)$, and the statistics of fully developed speckle.

A. A Complex Baseband Model for RF Ultrasound

From (30) we have:

$$r(x, y, t) \approx \iiint_{-\infty}^{+\infty} h(x' - x, y' - y, z', t) f_m(x', y', z') \, dx' dy' dz'.$$

We now form an analytic signal from the RF signal, using the Hilbert transform, $\mathcal{H}_t\{\bullet\}$ in the time dimension:

$$r(x, y, t) - j\mathcal{H}_t\{r(x, y, t)\} \approx \iiint_{-\infty}^{+\infty} \left[h(x' - x, y' - y, z', t) \right.$$

$$\left. - j\mathcal{H}_t\{h(x' - x, y' - y, z', t)\} \right] f_m(x', y', z') \, dx' \, dy' \, dz'. \tag{31}$$

If we assume that the center frequency of the RF ultrasound signal and the speed of sound in tissue are both reasonably constant, we can define a representation for the

complex analytic pulse in terms of its complex envelope, $\tilde{h}(x, y, z, t)$, the center frequency ω_0, and center wave number k_0:

$$h(x, y, z, t) - j\mathcal{H}_t\{h(x, y, z, t)\} = \tilde{h}(x, y, z, t) e^{j(\omega_0 t - 2k_0 z)}. \tag{32}$$

See Appendix C for a brief explanation of the factor of 2 in the exponent. The speed of ultrasound varies by up to 5% in different tissues. One material property, namely the sound speed, affects our measurement of another material property, the phase with which the ultrasound is backscattered. This is unavoidable in a baseband model in which $\tilde{h}$ is considered to be a property of the probe rather than the material being scanned. Typically, the center frequency of an RF scan line varies by less than 5% in the z direction, and this variation can be accommodated by the complex envelope $\tilde{h}$, which we have assumed to be spatially varying in this direction.

Therefore, we can rewrite (31) as:

$$r(x, y, t) - j\mathcal{H}_t\{r(x, y, t)\}$$

$$\approx \iiint_{-\infty}^{+\infty} \tilde{h}(x' - x, y' - y, z', t) e^{j(\omega_0 t - 2k_0 z')}$$

$$\times f_m(x', y', z') \, dx' \, dy' \, dz'$$

$$\approx e^{j\omega_0 t} \iiint_{-\infty}^{+\infty} \tilde{h}(x' - x, y' - y, z', t)$$

$$\times f_m(x', y', z') e^{-2jk_0 z'} \, dx' \, dy' \, dz'.$$

Hence:

$$[r(x, y, t) - j\mathcal{H}_t\{r(x, y, t)\}] e^{-j\omega_0 t} \approx$$

$$\iiint_{-\infty}^{+\infty} \tilde{h}(x' - x, y' - y, z', t) f_m(x', y', z') e^{-2jk_0 z'} \, dx' \, dy' \, dz'. \tag{33}$$

The left-hand side of (33) is the analytic RF signal with the high-frequency component at ω_0 removed. Let $\tilde{r}(x, y, t) = [r(x, y, t) - j\mathcal{H}_t\{r(x, y, t)\}] e^{-j\omega_0 t}$.

The term $f_m(x, y, z) e^{-2jk_0 z}$ is made up of $f_m(x, y, z)$, which is a real function of position, and $e^{-2jk_0 z}$, which determines the angle of the resulting complex number as a function of the remainder when the z position of the scatterer is divided by the wavelength, π/k_0, of the dominant frequency. For a 5 MHz probe, this wavelength is roughly 0.3 mm, so we can assume that, for diffuse scatterers, the scatterer position is random within the wavelength. This means that the phase of the scatterer is effectively uniformly distributed in the range 0 to 2π. Let $\tilde{f}_m(x, y, z) = f_m(x, y, z) e^{-2jk_0 z}$, a vector with magnitude determined by $f_m(x, y, z)$ and random phase.

Thus we now have an analogous complex equation to the real equation (30) in which: the high frequency components have been removed by demodulating with the pulse

center frequency, the pulse is now represented by a complex envelope analogous to the resolution cell of the imaging system, and the scatterers are represented by complex vectors of random phase:

$$\tilde{r}(x, y, t) \approx$$
$$\iiint\limits_{-\infty}^{+\infty} \tilde{h}\left(x' - x, y' - y, z', t\right) \tilde{f}_m\left(x', y', z'\right) dx'\, dy'\, dz', \quad (34)$$

where:

$\tilde{r}(x, y, t) =$ $[r(x, y, t) - j\mathcal{H}_t\{r(x, y, t)\}]\, e^{-j\omega_0 t}$, the analytic RF signal with the $e^{j\omega_0 t}$ component removed,

$\tilde{h}(x, y, z, t) =$ the complex envelope of the point spread function of the imaging system (i.e., the sensitivity to scatterers at the point (x, y, z) when forming the sum in $\tilde{r}$ for time t). Thus, this also can be viewed as the complex resolution cell or the complex pulse envelope relevant to the depth corresponding to time t.

$\tilde{f}_m(x, y, z) =$ the magnitude is from $f_m(x, y, z)$ and the phase from $e^{-2jk_0 z}$, so the phase is effectively random.

Note that we can calculate $\tilde{r}(x, y, t)$ from the measured RF signal, using an estimate of the pulse center frequency. If we get the center frequency slightly wrong, this will have the effect of reducing the smoothness of $\tilde{h}(x, y, z, t)$. This is illustrated using a simple example of an ultrasound pulse waveform, in Figs. 5 and 6. The analytic representation of the same pulse is shown in Figs. 5(a) and 6(a). In Fig. 5 the pulse is derotated by its mode frequency of 5.79 MHz, achieving a smooth envelope, which is shown in Fig. 5(c). In Fig. 6 the pulse is derotated by its mean frequency of 8.17 MHz. The asymmetry of the pulse's amplitude spectrum makes the mean frequency of 8.17 MHz less convenient to use for derotation in this case. Fig. 6(c) shows a pulse envelope that is not as smooth as Fig. 5(c). Notice that, in spite of the fact there is a significant difference between 5.79 MHz and 8.17 MHz, the signal in Fig. 6(c) is still sufficiently smooth to be used as a plausible pulse envelope.

B. Statistics of Speckle

The statistics of ultrasound images can indicate the type of scattering (specular/diffuse), the effective number of scatterers in each resolution cell, and any regularity in their spacing [16], [17]. Statistical information between neighboring RF images also can be used to measure the out-of-plane probe motion [18], [19]. As a starting point, it, therefore, is useful to analyze the ideal case of fully developed speckle, in which there are a large number of scatterers (at least 30 so the central limit theorem will hold) within the resolution cell.

In all our discussion of speckle statistics, we assume, without loss of generality, that we are working at a particular depth corresponding to the time t in the RF signal $\tilde{r}$.

From (34) we can see that each value in $\tilde{r}$ is formed from the sum of all the scatterers within the pulse envelope. Provided this envelope extends over more than one wavelength (π/k_0), we can assume that the scatterers have effectively random phase derived from the $\tilde{f}_m$ term. If there are a large number of scatterers within the pulse envelope, by the central limit theorem, the vector sum of these complex numbers will be distributed as a two-dimensional Gaussian in the Argand diagram:

$$\mathbf{Pr}(\tilde{r}) = \frac{1}{2\pi\sigma^2} \exp\left[\frac{-\Re(\tilde{r})^2 - \Im(\tilde{r})^2}{2\sigma^2}\right],$$

where:

$\mathbf{Pr}(\tilde{r}) =$ the probability density function of $\tilde{r}$,

$\Re(\tilde{r}) =$ the real part of $\tilde{r}$,

$\Im(\tilde{r}) =$ the imaginary part of $\tilde{r}$,

$$2\sigma^2 = \langle f_m^2 \rangle \iiint\limits_{-\infty}^{+\infty} \left[\tilde{h}(x, y, z, t)\right]^2 dx\, dy\, dz,$$

$\langle \bullet \rangle$ denotes the expected value of a quantity. Note that the resolution cell $\tilde{h}$ varies with depth. To calculate σ, we take the energy under the curve relevant to a depth given by time t in the RF signal. To find the amplitude distribution $|\tilde{r}|$, we express $\tilde{r}$ in polar coordinates and integrate over all angles:

$$\tilde{r} = \Re(\tilde{r}) + j\Im(\tilde{r}) = |\tilde{r}|e^{j\theta}$$

$$\Rightarrow \mathbf{Pr}(\tilde{r}) = \frac{1}{2\pi\sigma^2} \exp\left(\frac{-|\tilde{r}|^2}{2\sigma^2}\right)$$

$$\Rightarrow \mathbf{Pr}(|\tilde{r}|) = \int_0^{2\pi} \mathbf{Pr}(\tilde{r})\, d\theta = \frac{2\pi|\tilde{r}|}{2\pi\sigma^2} \exp\left(\frac{-|\tilde{r}|^2}{2\sigma^2}\right)$$

$$= \frac{|\tilde{r}|}{\sigma^2} \exp\left(\frac{-|\tilde{r}|^2}{2\sigma^2}\right).$$

This gives us a Rayleigh distribution, as expected.

Now introduce variables to represent the amplitude and intensity of the backscattered signal:

$$A = |\tilde{r}| \quad \text{(the amplitude)},$$
$$I = A^2 \quad \text{(the intensity)}.$$

As already mentioned, the amplitude is Rayleigh distributed. The intensity follows an exponential distribution:

$$\mathbf{Pr}(A) = \frac{A}{\sigma^2} \exp\left(\frac{-A^2}{2\sigma^2}\right),$$

$$\mathbf{Pr}(I) = \frac{1}{2\sigma^2} \exp\left(\frac{-I}{2\sigma^2}\right).$$

Also $\langle A \rangle = \sigma\sqrt{\frac{\pi}{2}}$, $\langle A^2 \rangle = \langle I \rangle = 2\sigma^2$ and $\langle I^2 \rangle = 8\sigma^4$.

C. Second Order Statistics of Speckle

Consider two points in space, labeled 1 and 2. They are located inside an ultrasound phantom that generates a
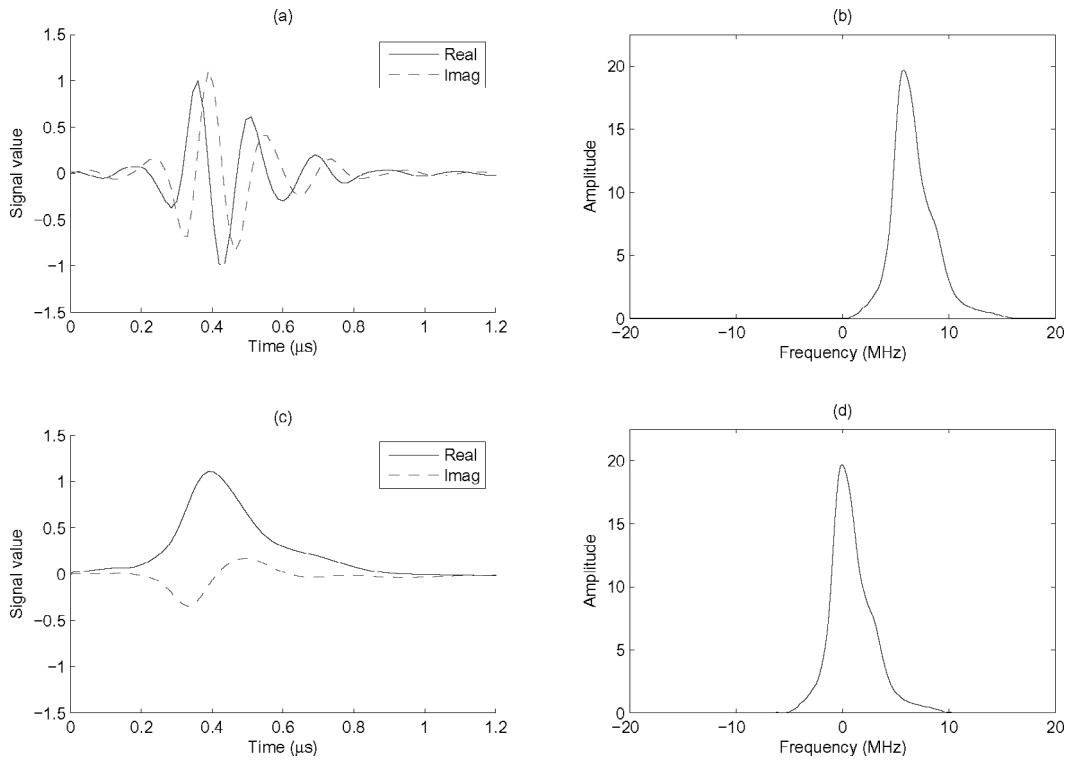
Fig. 5. An analytic RF pulse derotated by its mode frequency of 5.79 MHz. (a) Real RF pulse and corresponding imaginary signal, computed using a Hilbert transform. (b) Amplitude spectrum of the pulse. (c) Pulse after multiplication by a sinusoid at 5.79 MHz. (d) Amplitude spectrum of (c). The vertical axes on all the graphs are in arbitrary units.
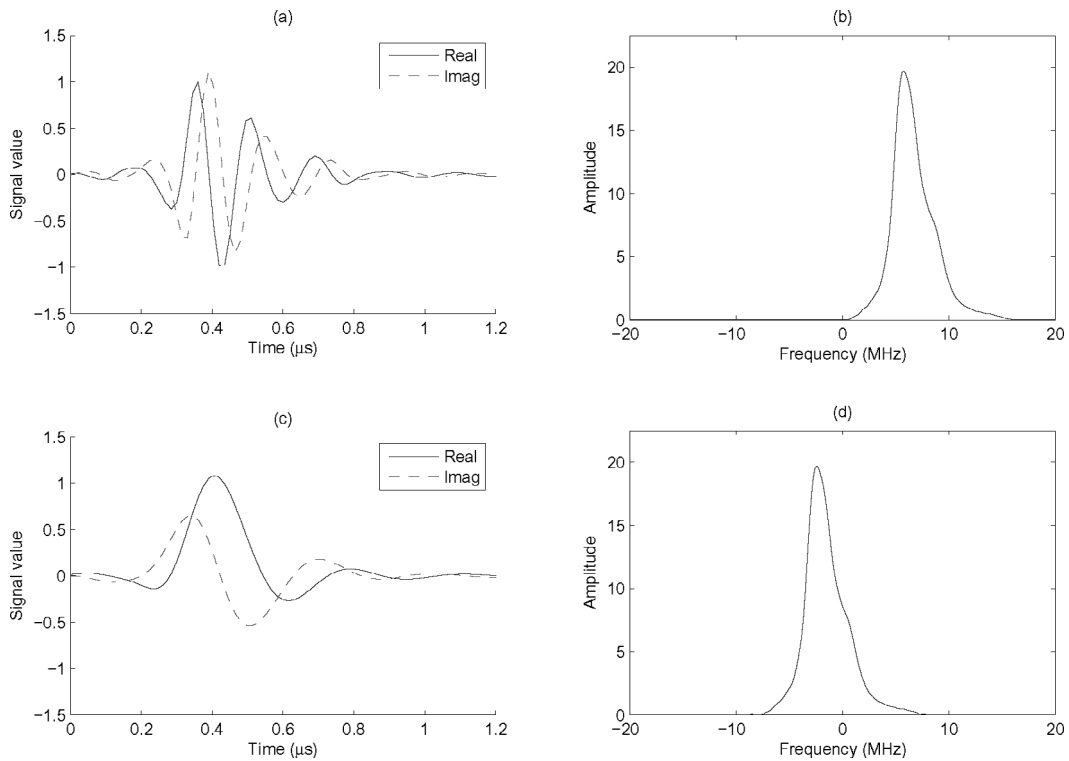

Fig. 6. An analytic RF pulse derotated by its mean frequency of 8.17 MHz. (a) Real RF pulse and corresponding imaginary signal, computed using a Hilbert transform. (b) Amplitude spectrum of the pulse. (c) Pulse after multiplication by a sinusoid at 8.17 MHz. (d) Amplitude spectrum of (c). The vertical axes on all the graphs are in arbitrary units.

fully-developed speckle backscatter signal. Point 1 is at position (x_1, y_1, z_1) and point 2 is at position $(x_1 + \delta_x, y_1, z_1)$. Quantities at points 1 and 2 will be denoted using subscripts, for example A_1 is the amplitude at point 1.

Following equation 35 of [20], define λ as the magnitude of the normalized covariance of $\tilde{r}$:

$$\lambda = \frac{|\langle \tilde{r}_1 \tilde{r}_2^* \rangle|}{2\sigma^2}.$$

We assume that the resolution cell (point spread function) of the ultrasound scanner is an even function in the x direction: $\tilde{h}(x, y, z, t)$. Drawing on results from [19], as detailed in Appendix D, we can directly obtain a convenient expression for λ in terms of the overlap of the resolution cells at points 1 and 2:

$$\lambda = 1 - \frac{\overset{+\infty}{\underset{-\infty}{\iiint}} \left[\tilde{h}(x + \delta_x, y, z, t) - \tilde{h}(x, y, z, t) \right]^2 \, dx \, dy \, dz}{2 \overset{+\infty}{\underset{-\infty}{\iiint}} \left[\tilde{h}(x, y, z, t) \right]^2 \, dx \, dy \, dz}. \tag{35}$$

The integrals in (35) are over the spatial dimensions x, y, and z; thus, it is expressing λ in terms of the resolution cell (or spatial sensitivity function [3]). This resolution cell $\tilde{h}$ varies slowly with depth. As $\tilde{h}$ does not generally extend over a wide range of z values for any particular value of t, this expression is valid at any depth, provided $\tilde{h}$ is evaluated with the appropriate value of t. Therefore, it is often possible to use an approximation based on the PSF and evaluate the integrals in (35) over x, y, and t for a given z.

We show later in this section that the second order statistics of speckle can be calculated directly from λ. Thus (35) provides a convenient link between techniques for calculating [21] or estimating [22], [23] the resolution cell, and work that makes use of the speckle statistics for distance measurement in free-hand, three-dimensional ultrasound [19], [24].

If $\tilde{h}$ is a three-dimensional Gaussian with standard deviation width in the x direction equal to w_x:

$$\tilde{h}(x, y, z, t) \propto \frac{1}{w_x w_y w_z (2\pi)^{\frac{3}{2}}} \exp \left[-\frac{x^2}{2w_x^2} - \frac{y^2}{2w_y^2} - \frac{\left(z - \frac{\omega t}{2k} \right)^2}{2w_z^2} \right],$$

then (35) evaluates to:

$$\lambda^2 = \exp \left(\frac{-\delta_x^2}{2w_x^2} \right). \tag{36}$$

Note that the parameters of $\tilde{h}(x, y, z, t)$, i.e., w_x, w_y, k, ω, and w_z will all vary slowly as a function of t. We have reported simulations and experiments showing the use of this equation previously [19].

From [5], [19], [25], the expected value of the products $I_1 I_2$ and $A_1 A_2$ are:

$$\langle I_1 I_2 \rangle = 4\sigma^4 \left(1 + \lambda^2 \right),$$

$$\langle A_1 A_2 \rangle = \frac{\pi \sigma^2}{2} \, _2F_1 \left(-\tfrac{1}{2}, -\tfrac{1}{2}; 1; \lambda^2 \right)$$

$$= \sigma^2 \left[2E(\lambda^2) - \left(1 - \lambda^2 \right) K(\lambda^2) \right],$$

where $_2F_1(\bullet)$ is the Gaussian hypergeometric function [25], [26], and $K(\bullet)$ and $E(\bullet)$ are the complete elliptic integrals of the first and second kinds, respectively. Following [26], we have adopted the convention that the arguments of $K(\bullet)$ and $E(\bullet)$ are given as the parameter (conventionally $K(m)$ and $E(m)$) rather than the modulus (conventionally $K(k)$ and $E(k)$ where $k^2 = m$). Other authors [5], [25], have chosen the alternate definition for these functions. Algorithms for evaluating the elliptic integrals are available in [26], and packages like Matlab (Mathworks Inc., Natick, MA) provide functions to compute them.

The Pearson correlation coefficient is defined:

$$\rho(p, q) = \frac{\langle pq \rangle - \langle p \rangle \langle q \rangle}{\sqrt{\langle p^2 \rangle - \langle p \rangle^2} \sqrt{\langle q^2 \rangle - \langle q \rangle^2}}. \tag{37}$$

Using (35) or (36) to determine λ, we thus can calculate the Pearson correlation coefficients of amplitude and intensity values separated by a distance δ_x in the x direction:

$$\rho(I_1, I_2) = \lambda^2, \tag{38}$$

$$\rho(A_1, A_2) = \frac{4E(\lambda^2) - 2 \left(1 - \lambda^2 \right) K(\lambda^2) - \pi}{4 - \pi}. \tag{39}$$

If we assume that the complex resolution cell varies only slowly with depth, these formulae are valid for displacements in any direction, not just in the x direction as described above.

Most of the results in Section V-B and V-C are drawn from previous papers (e.g., [4], [5]), but we believe (35), that relates λ to the overlap of the complex resolution cells, has not been previously published in this form.

VI. DISCUSSION

The major assumption underpinning this model is that of weak scattering; in our analysis, we showed that this means requiring the scattering to be weak enough that multiple scattering can be ignored. Most authors acknowledge that weak scattering occurs when the scatterers' acoustic properties differ from the medium's by small amounts [1], [2], [9], but they overlooked the fact that weak scattering also occurs when the size of the scatterers is very small compared to the wavelength of the incident wave, irrespective of the acoustic properties of the scatterers. At such small dimensions, the shape of the scatterers may be assumed to be spherical [27] and, for a rigid sphere, the total power scattered is very small when the radius of the sphere is much less than $\frac{\lambda}{2\pi}$ [9].

In human tissue, the assumption of weak scattering does not hold at strongly, reflecting interfaces such as organ boundaries. Cho *et al.* [28], however, have suggested that it is possible to extend the linear model's validity beyond the Born approximation regime by modifying the PSF to account for some degree of multiple scattering.

The other significant limitation on our linear model is the approximation inherent in (20). From a systems' point-of-view, the monopole and dipole terms $\gamma(\mathbf{x})$ and $\mu(\mathbf{x})$ are in fact two separate input signals contributing to the force on the receive subaperture (and therefore to the RF trace). The spatiotemporal filters applied by the physics of the system to each of these input signals are different; it is only at distances larger than the diameter of the transmit and receive subapertures that the responses of these spatiotemporal filters become sufficiently similar (in magnitude) to allow $\gamma(\mathbf{x})$ and $\mu(\mathbf{x})$ to be combined into the single quantity $f_m(\mathbf{x})$. Of course, when one of the inputs is significantly larger than the other (i.e., when only one of monopole or dipole scattering is dominant), then we may approximate this physical behavior as a single-input, single-output linear system without this large distance constraint.

VII. CONCLUSIONS

We have shown how the expression for the RF signal in terms of the scatterer field and a spatially varying PSF can be transformed into a representation in terms of complex analytic signals. The complex model incorporates a spatially varying complex PSF envelope that takes account of variations in the shape of the real PSF as well as changes in the speed of sound and the center frequency of the backscattered signal.

It is easier to perform simulation and analysis of ultrasound scattering using this complex representation than using RF signals because accurate modeling of spatial variation on the scale of a wavelength is not necessary, and the various quantities do not vary at RF frequencies and, hence, can be sampled more sparsely. Our approach provides a direct interpretation of the complex quantities in terms of their RF analogues and thus makes it easier to understand the physical significance of results. We show how the complex representation easily can be used to derive the first and second order statistics of fully developed speckle.

APPENDIX A
PROOF OF (17)

For convenience, we restate (17):

$$\int_{\mathsf{R}^3} \nabla \cdot \left[\mu(\mathbf{x}) \left(\nabla H_t \right) (\mathbf{x}, \omega) \right] H_r(\mathbf{x}, \omega) d^3\mathbf{x} =$$
$$- \int_{\mathsf{R}^3} \mu(\mathbf{x}) \left(\nabla H_t \cdot \nabla H_r \right) (\mathbf{x}, \omega) \, d^3\mathbf{x}.$$

Proof: This proof is taken from [9]. Let $\mathbf{A}(\mathbf{x}) = \nabla \cdot \left[\mu(\mathbf{x}) \left(\nabla H_t \right) (\mathbf{x}, \omega) \right]$ and $b(\mathbf{x}) = H_r(\mathbf{x}, \omega)$. We begin with the identity:

$$b(\mathbf{x}) \nabla \cdot \mathbf{A}(\mathbf{x}) = -\mathbf{A}(\mathbf{x}) \cdot \nabla b(\mathbf{x}) + \nabla \cdot \left[b(\mathbf{x}) \mathbf{A}(\mathbf{x}) \right],$$
(40)

which can be verified by expanding the RHS and simplifying. Let $\mathcal{V}'$ be the volume within which $\mathbf{A}(\mathbf{x})$ is nonzero, i.e., $\mathbf{A}(\mathbf{x}) = \mathbf{0}$ for $\mathbf{x} \notin \mathcal{V}'$. Integrating both sides over $\mathcal{V}'$:

$$\int_{\mathcal{V}'} b(\mathbf{x}) \nabla \cdot \mathbf{A}(\mathbf{x}) d^3\mathbf{x} = - \int_{\mathcal{V}'} \mathbf{A}(\mathbf{x}) \cdot \nabla b(\mathbf{x}) d^3\mathbf{x}$$
$$+ \int_{\mathcal{V}'} \nabla \cdot \left[b(\mathbf{x}) \mathbf{A}(\mathbf{x}) \right] d^3\mathbf{x}. \quad (41)$$

By the divergence theorem [29], the second integral on the RHS is equal to the surface integral $\oint_{\mathcal{S}'} b(\mathbf{x}) \mathbf{A}(\mathbf{x}) \cdot \hat{\mathbf{n}}(\mathbf{x}) d^2\mathbf{x}$, where $\mathcal{S}'$ is some surface enclosing $\mathcal{V}'$ and $\hat{\mathbf{n}}(\mathbf{x})$ is a unit vector normal to $\mathcal{S}'$. Because $\mathbf{A}(\mathbf{x})$ is zero outside $\mathcal{V}'$, the surface integral reduces to zero and (17) follows.

APPENDIX B
PROOF OF (19)

For convenience, we restate (19):

$$\left(\nabla H_t \cdot \nabla H_r \right) (\mathbf{x}, \omega) \approx - \left(\frac{\omega}{c_0} \right)^2 H_t(\mathbf{x}, \omega) H_r(\mathbf{x}, \omega).$$

Proof: We define the wave vector $\mathbf{k} = \frac{\omega}{c_0} \hat{\mathbf{r}}$, where $\hat{\mathbf{r}} = \frac{\mathbf{x} - \mathbf{x_a}}{|\mathbf{x} - \mathbf{x_a}|}$; in other words, $\hat{\mathbf{r}}$ is a unit vector parallel to $\mathbf{x} - \mathbf{x_a}$ and $\mathbf{k}$ is a vector also parallel to $\mathbf{x} - \mathbf{x_a}$ but with magnitude $\frac{\omega}{c_0}$. We then can rewrite (7) for the transmit transfer function as:

$$H_t(\mathbf{x}, \omega) = \int_{\mathcal{A}} V(\mathbf{x_a}, \omega) \frac{e^{-j\mathbf{k} \cdot (\mathbf{x} - \mathbf{x_a})}}{2\pi |\mathbf{x} - \mathbf{x_a}|} d^2\mathbf{x_a}.$$
(42)

Taking the gradient (43) (see next page), we apply the condition $\frac{1}{|\mathbf{x} - \mathbf{x_a}|} \ll |\mathbf{k}| = \frac{\omega}{c_0}$, i.e., $|\mathbf{x} - \mathbf{x_a}| \gg \frac{c_0}{\omega}$. (43) then reduces to:

$$\left(\nabla H_t \right) (\mathbf{x}, \omega) \approx \int_{\mathcal{A}} V(\mathbf{x_a}, \omega) \frac{e^{-j\mathbf{k} \cdot (\mathbf{x} - \mathbf{x_a})}}{2\pi |\mathbf{x} - \mathbf{x_a}|} (-j\mathbf{k}) d^2\mathbf{x_a}.$$
(44)

We also assume that the direction of $\mathbf{k}$ does not vary very much over the transmit subaperture which allows the $-j\mathbf{k}$ term on the RHS to be factored out of the integral:

$$\left(\nabla H_t \right) (\mathbf{x}, \omega) \approx -j\mathbf{k} \int_{\mathcal{A}} V(\mathbf{x_a}, \omega) \frac{e^{-j\mathbf{k} \cdot (\mathbf{x} - \mathbf{x_a})}}{2\pi |\mathbf{x} - \mathbf{x_a}|} d^2\mathbf{x_a}$$
$$\approx -j\mathbf{k} H_t(\mathbf{x}, \omega). \quad (45)$$

By an identical process, we obtain, for the receive-transfer function:

$$\left(\nabla H_r \right) (\mathbf{x}, \omega) \approx -j\mathbf{k} H_r(\mathbf{x}, \omega),$$
(46)

taking the dot product of (45) and (46) yields (19).

In practice, the condition $|\mathbf{x} - \mathbf{x_a}| \gg \frac{c_0}{\omega}$ is satisfied for virtually the entire imaged region because the wavelengths from medical ultrasound probes are usually very short. For example, consider a typical probe transmitting
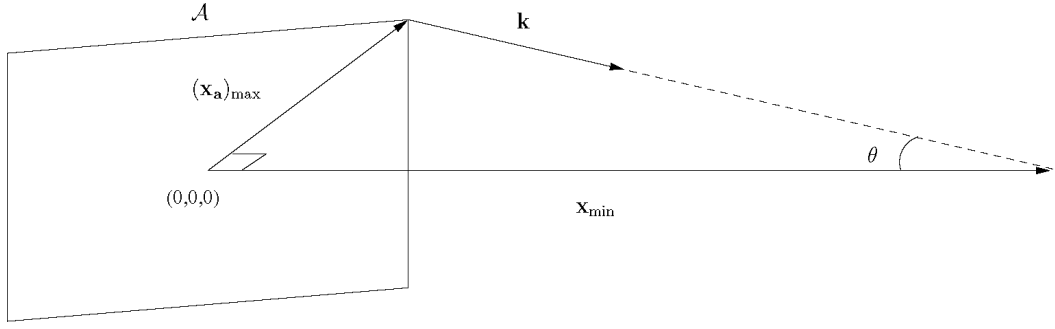
Fig. 7. Coordinate system for calculating an approximation to $(\nabla H_t \cdot \nabla H_r)(\mathbf{x}, \omega)$.

$$
\begin{aligned}
(\nabla H_t)(\mathbf{x}, \omega) &= \frac{1}{2\pi} \int_{\mathcal{A}} V(\mathbf{x_a}, \omega) \nabla \left[\frac{e^{-j\mathbf{k} \cdot (\mathbf{x} - \mathbf{x_a})}}{|\mathbf{x} - \mathbf{x_a}|} \right] d^2\mathbf{x_a} \\
&= \frac{1}{2\pi} \int_{\mathcal{A}} V(\mathbf{x_a}, \omega) \left[\frac{\nabla e^{-j\mathbf{k} \cdot (\mathbf{x} - \mathbf{x_a})}}{|\mathbf{x} - \mathbf{x_a}|} + e^{-j\mathbf{k} \cdot (\mathbf{x} - \mathbf{x_a})} \nabla \left(\frac{1}{|\mathbf{x} - \mathbf{x_a}|} \right) \right] d^2\mathbf{x_a} \\
&= \frac{1}{2\pi} \int_{\mathcal{A}} V(\mathbf{x_a}, \omega) \left[-j\mathbf{k} \frac{e^{-j\mathbf{k} \cdot (\mathbf{x} - \mathbf{x_a})}}{|\mathbf{x} - \mathbf{x_a}|} - \frac{e^{-j\mathbf{k} \cdot (\mathbf{x} - \mathbf{x_a})}}{|\mathbf{x} - \mathbf{x_a}|^2} \hat{\mathbf{r}} \right] d^2\mathbf{x_a} \\
&= \frac{1}{2\pi} \int_{\mathcal{A}} V(\mathbf{x_a}, \omega) \frac{e^{-j\mathbf{k} \cdot (\mathbf{x} - \mathbf{x_a})}}{|\mathbf{x} - \mathbf{x_a}|} \left(-j\mathbf{k} - \frac{\hat{\mathbf{r}}}{|\mathbf{x} - \mathbf{x_a}|} \right) d^2\mathbf{x_a},
\end{aligned}
\tag{43}
$$

at 6.5 MHz into human tissue that has an average speed of sound of 1540 m/s. For this probe, $\frac{c_0}{\omega}$ has an average value of 0.0377 mm, which is practically negligible.

The condition that the direction of $\mathbf{k}$ not vary very much over the transmit and receive subapertures is much stricter and is only satisfied in regions far away from $\mathcal{A}$. To quantify exactly what is meant by far away, we consider the setup of Fig. 7.

For a typical focused probe, we expect the majority of the transmitted acoustic energy to be concentrated in a small region enclosing the axial axis, and so we have chosen to consider only the scenario in which $\mathbf{x}$ lies along this axis. We can restate our requirement that $\mathbf{k}$ be uniform over $\mathcal{A}$ by equivalently requiring $\mathbf{k}$ to be approximately parallel to $\mathbf{x}$.

This requirement is most difficult to satisfy when we consider the point on $\mathcal{A}$ farthest from the center of $\mathcal{A}$, i.e., when $\mathbf{x_a} = (\mathbf{x_a})_{\max}$. Our requirement that $\mathbf{k}$ be approximately parallel to $\mathbf{x}$ can be stated in terms of the dot product as $\mathbf{k} \cdot \mathbf{x} \approx |\mathbf{k}| |\mathbf{x}|$; in the case in which $\mathbf{x_a} = (\mathbf{x_a})_{\max}$ (as shown in Fig. 7), we require $\cos \theta \approx 1$. If we allow a 10% error in this approximation for $\cos \theta$, we effectively impose the constraint $\cos \theta > 0.9 \Rightarrow \theta < 26°$. From Fig. 7, $|\mathbf{x}_{\min}| = |(\mathbf{x_a})_{\max}| \cot \theta$ and so our requirement that $\theta < 26°$ translates to requiring $|\mathbf{x}| > 2 |(\mathbf{x_a})_{\max}|$.

What we have demonstrated in this brief discussion is that the approximation in (19) is satisfied well at axial depths that are greater than the diameter of $\mathcal{A}$ (for non-circular $\mathcal{A}$, this diameter is the diameter of the smallest circle within which $\mathcal{A}$ can be inscribed). The same claim is made without proof in [11].

APPENDIX C
MOTIVATION FOR (32)

Consider a pulse P of an unspecified complex quantity propagating into a medium in the z direction at speed ω/k:

$$ P(\omega t - kz). $$

It is reflected at a depth z_1 and travels back in the $-z$ direction. Changes in phase and amplitude during the reflection are represented by q_1. The reflected pulse is:

$$ q_1 P(\omega t + (z - z_1) k - z_1 k). $$

When this pulse gets back to the probe (i.e., $z = 0$), we have:

$$ q_1 P(\omega t - 2kz_1). $$

Hence, we represent $h(x, y, z, t) - j\mathcal{H}_t\{h(x, y, z, t)\}$ as $\tilde{h}(x, y, z, t) e^{j(\omega_0 t - 2k_0 z)}$ in (32).

APPENDIX D
PROOF OF (35)

For convenience, we restate (35):

$$
\lambda = 1 - \frac{\iiint\limits_{-\infty}^{+\infty} \left[\tilde{h}(x + \delta_x, y, z, t) - \tilde{h}(x, y, z, t) \right]^2 dx \, dy \, dz}{2 \iiint\limits_{-\infty}^{+\infty} \left[\tilde{h}(x, y, z, t) \right]^2 dx \, dy \, dz}.
$$

Proof: We start by reproducing equation 35 from [20] in our notation, and introduce a modulus sign as the analytic signal can otherwise result in a complex value (as noted in the comment below equation 36 in [20]).

$$\lambda = \frac{|\langle \tilde{r}_1 \tilde{r}_2^* \rangle|}{2\sigma^2}$$

Using equation 18 from [5] together with the definition of the Pearson correlation coefficient in (37), we can compute (38) in the main text of this paper:

$$\rho(I_1, I_2) = \lambda^2. \tag{47}$$

Equation A.6 in [19] is:

$$\rho(I_1, I_2) = b, \tag{48}$$

(the reader is referred to [19] for the definition of b) and equation 14 from [19] is:

$$b = \left(1 - \frac{\langle i \rangle}{\langle I \rangle}\right)^2. \tag{49}$$

Combining (47), (48), and (49) gives us:

$$\lambda = 1 - \frac{\langle i \rangle}{\langle I \rangle}. \tag{50}$$

The quantities $\langle i \rangle$ and $\langle I \rangle$, which are defined in [19], can be expressed in terms of the complex resolution cell $\tilde{h}$ using equations 21 and 22 from [19]:

$$\langle I \rangle = k^2 \iiint\limits_{-\infty}^{+\infty} \left[\tilde{h}(x,y,z,t)\right]^2 \, dx\, dy\, dz,$$

$$\langle i \rangle = \frac{1}{2} k^2 \iiint\limits_{-\infty}^{+\infty} \left[\tilde{h}(x + \delta_x, y, z, t) - \tilde{h}(x,y,z,t)\right]^2 \, dx\, dy\, dz,$$

where k^2 represents the average backscattering intensity. We can substitute these expressions into (50) and cancel k^2, to give (35).

Acknowledgments

The authors would like to thank Julian Sonner for helpful discussions on wave propagation and the solution of the wave equation.

References

[1] J. Gore and S. Leeman, "Ultrasonic backscattering from human tissue: A realistic model," *Phys. Med. Biol.*, vol. 22, no. 2, pp. 317–326, 1977.

[2] J. A. Jensen, "A model for the propagation and scattering of ultrasound in tissue," *J. Acoust. Soc. Amer.*, vol. 89, pp. 182–190, Jan. 1991.

[3] R. J. Zemp, C. K. Abbey, and M. F. Insana, "Linear system models for ultrasonic imaging: Application to signal statistics," *IEEE Trans. Ultrason., Ferroelect., Freq. Contr.*, vol. 50, no. 6, pp. 642–654, June 2003.

[4] C. B. Burckhardt, "Speckle in ultrasound B-mode scans," *IEEE Trans. Sonics Ultrason.*, vol. SU-25, pp. 1–6, Jan. 1978.

[5] R. F. Wagner, S. W. Smith, J. M. Sandrik, and H. Lopez, "Statistics of speckle in ultrasound B-scan," *IEEE Trans. Sonics Ultrason.*, vol. SU-30, pp. 156–163, May 1983.

[6] K. A. Wear, R. Wagner, and D. G. Brown, "Statistical properties of estimates of signal-to-noise ratio and number of scatterers per resolution cell," *J. Acoust. Soc. Amer.*, vol. 102, pp. 635–641, July 1997.

[7] P. N. T. Wells and M. Halliwell, "Speckle in ultrasonic imaging," *Ultrasonics*, vol. 19, pp. 225–229, Sep. 1981.

[8] J. Goodman, "Statistical properties of laser speckle patterns," in *Laser Speckle and Related Phenomena*. J. Dainty, Ed. Berlin: Springer-Verlag, 1975.

[9] P. M. Morse and K. U. Ingard, *Theoretical Acoustics*. New York: McGraw-Hill, 1968.

[10] G. F. Carrier and C. E. Pearson, *Partial Differential Equations: Theory and Technique*. New York: Academic, 1976.

[11] M. F. Insana, R. F. Wagner, D. G. Brown, and T. J. Hall, "Describing small-scale structure in random media using pulse-echo ultrasound," *J. Acoust. Soc. Amer.*, vol. 87, pp. 179–192, Jan. 1990.

[12] A. D. Pierce, *Acoustics: An Introduction to Its Physical Principles and Applications*. New York: McGraw-Hill, 1981.

[13] L. J. Ziomek, *Fundamentals of Acoustic Field Theory and Space-Time Signal Processing*. Boca Raton, FL: CRC Press, 1995.

[14] W. F. Walker, "C- and d-weighted ultrasonic imaging using the translating apertures algorithm," *IEEE Trans. Ultrason., Ferroelect., Freq. Contr.*, vol. 48, pp. 452–461, Mar. 2001.

[15] J. A. Jensen, "Field: A program for simulating ultrasound systems," in *Proc. 10th Nordic-Baltic Conf. Biomed. Imag. Med. Biol. Eng. Comput. Tampere*, 1996, pp. 351–353.

[16] V. Dutt and J. F. Greenleaf, "Ultrasound echo envelope analysis using a homodyned k distribution signal model," *Ultrason. Imag.*, vol. 16, pp. 265–287, 1994.

[17] G. Georgiou and F. S. Cohen, "Statistical characterization of diffuse scattering in ultrasound images," *IEEE Trans. Ultrason., Ferroelect., Freq. Contr.*, vol. 45, pp. 57–64, Jan. 1998.

[18] T. A. Tuthill, J. F. Krücker, J. B. Fowlkes, and P. L. Carson, "Automated three-dimensional US frame positioning computed from elevational speckle decorrelation," *Radiology*, vol. 209, pp. 575–582, 1998.

[19] R. W. Prager, A. H. Gee, G. M. Treece, C. J. C. Cash, and L. H. Berman, "Sensorless freehand 3D ultrasound using regression of the echo intensity," *Ultrasound Med. Biol.*, vol. 29, pp. 437–446, Mar. 2003.

[20] R. Wagner, M. F. Insana, and D. G. Brown, "Statistical properties of radio-frequency and envelope-detected signals with applications to medical ultrasound," *J. Opt. Soc. Amer. A*, vol. 4, pp. 910–922, May 1987.

[21] J. A. Jensen, "Estimation of pulses in ultrasound B-scan images," *IEEE Trans. Med. Imag.*, vol. 10, pp. 164–172, June 1991.

[22] T. Taxt and J. Strand, "Two-dimensional noise-robust blind deconvolution of ultrasound images," *IEEE Trans. Ultrason., Ferroelect., Freq. Contr.*, vol. 48, pp. 861–866, July 2001.

[23] J. K. H. Ng, R. W. Prager, N. G. Kingsbury, G. M. Treece, and A. H. Gee, "Tomographic reconstruction of the point-spread function of an ultrasonic imaging system for deconvolution," Cambridge Univ. Department of Engineering, Cambridge, UK, Technical Report CUED/F-INFENG/TR 529, 2005.

[24] P. Hassenpflug, R. W. Prager, G. M. Treece, and A. H. Gee, "Distance measurement for sensorless 3D ultrasound," in *Proc. Med. Image Comput. Computer-Assisted Intervention*, Sep. 2004, pp. 1087–1188.

[25] D. Middleton, *An Introduction to Statistical Communication Theory*. New York: McGraw-Hill, 1960.

[26] M. Abramowitz and I. A. Stegun, *Handbook of Mathematical Functions*. New York: Dover, 1970.

[27] V. Shutilov, *Fundamental Physics of Ultrasound*. New York: Gordon and Breach, 1988.

[28] Z.-H. Cho, J. P. Jones, and M. Singh, *Foundations of Medical Imaging*. New York: Wiley, 1993.

[29] K. Riley, M. Hobson, and S. Bence, *Mathematical Methods for Physics and Engineering*. 2nd ed. Cambridge, UK: Cambridge Univ. Press, 2002.
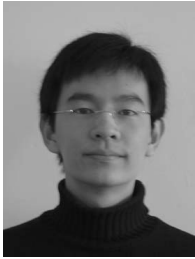
James Ng was born in Kuala Lumpur, Malaysia, in 1981. From 1999 to 2002 he studied at the University of Auckland, New Zealand, obtaining the B.E. (Hons) degree in computer systems engineering in May 2003. He currently holds an external research studentship from Trinity College, Cambridge, UK, and an LB Wood Travelling Scholarship. Since October 2003, he has been conducting research toward the Ph.D. degree at the Department of Engineering, Cambridge University.

His research interests are in image processing, complex wavelets and inverse problems. He is at present working on Bayesian methods for the restoration of medical ultrasound images.

Richard Prager received the B.A. degree in electrical sciences in 1984 and the Ph.D. degree in information engineering in 1987, both from Cambridge University, Cambridge, UK. He was elected to a Fellowship at Queens' College, Cambridge, in 1988. In the Engineering Department of Cambridge University he was appointed senior assistant in research in 1989, lecturer in 1992, senior lecturer in 2000, and reader in information engineering in 2002.

From 1996 to 1999 he held the post of Director of Undergraduate Education, and in 2001 he was awarded the Pilkington Prize for excellence in teaching by the Trustees of the Cambridge Foundation. His research interests are in medical imaging, and include acquisition and use of radiofrequency, three-dimensional ultrasound. He is one of the principle architects of both the Stradx and Stradwin freehand 3-D ultrasound systems. He is a Chartered Engineer (CEng) through membership of the Institute of Electrical Engineers.

Nick Kingsbury (M'87) received the honours degree in 1970 and the Ph.D. degree in 1974, both in electrical engineering from the University of Cambridge.

From 1973 to 1983 he was a design engineer and subsequently a group leader with Marconi Space and Defence Systems, Portsmouth, England, specializing in digital signal processing and coding as applied to speech coders, spread spectrum satcomms, and advanced radio systems. Since 1983 he has been a lecturer in communications systems and image processing at the University of Cambridge and a Fellow of Trinity College, Cambridge. He was appointed to a Readership in Signal Processing at Cambridge in 2000.

His current research interests include image compression, error-robust source coding techniques, and image analysis and enhancement techniques, particularly those based on wavelet decompositions. He has developed the dual-tree complex wavelet transform and is especially interested in the application of complex wavelets to the analysis of images and 3-D datasets. He is a member of the IEEE.

Graham Treece was awarded a first class B.A. degree in engineering, with distinction, from the University of Cambridge, Cambridge, UK, in 1993. From 1994 to 1995 he worked for Noise Cancellation Technologies Ltd., Cambridge, UK, designing active noise cancellation prototypes for cars and trucks. After this, he was employed by Plextek Ltd., Great Chesterford, Essex, UK, a leading independent design consultancy specializing in microelectronics and communications, as a real-time embedded software engineer. In 1997 he returned to Cambridge University and received his Ph.D. degree on volume measurement and surface visualization in 3-D ultrasound in June 2001. Since then he has continued to work in this area, initially as a research associate. In October 2003 he was awarded a research fellowship from the Royal Academy of Engineering and the Engineering and Physical Sciences Research Council in the UK. He is also a Fellow of Queens' College, Cambridge.

His current research interests are in visualization, system design, and the reduction of artefacts in 3-D ultrasound. He is one of the authors of the Stradx 3-D ultrasound system, widely recognized as state-of-the-art. He also has research interests in medical imaging and computer graphics, particularly surface visualization.

Andrew Gee obtained a B.A. degree in electrical and information science at Cambridge University, Cambridge, UK, in 1990. He was awarded the Ph.D. degree in 1993 from the same university for his thesis on the use of feedback neural networks for combinatorial optimization.

In 1993, he was appointed to a Research Fellowship at Queens' College, Cambridge, where he started to work on computer vision. In October 1995 he became an assistant lecturer in information engineering and an official fellow of Queens' College, Cambridge, UK, where he is now Director of Studies in Engineering. He was promoted to the post of lecturer in January 1998 and senior lecturer in October 2001. He teaches undergraduate courses in all aspects of computing. In 1998 he was awarded a Pilkington Prize by the Trustees of the Cambridge Foundation for excellence in teaching at the University of Cambridge.

He has worked in a number of research areas, including medical imaging, computer vision, document image processing and neural networks. Currently, he is working on aspects of 3-D ultrasound and related topics in computer graphics. He has authored and co-authored about 100 papers.